Revision 2

Melting phase equilibrium relations in the $MgSiO_3$–SiO_2 system under high pressures

Takuya Moriguti[1*], Yusuke Yachi[1], Akira Yoneda[1, 2], and Eiji Ito[1]

[1]Institute for Planetary Materials, Okayama University, Misasa, Tottori 682-0193, Japan.

[2]Department of Earth and Space Science, Graduate School of Science, Osaka University, Toyonaka, Osaka 560-0043, Japan

*Corresponding author

email:moriguti@misasa.okayama-u.ac.jp

Submitted this revision to American Mineralogist

November 25, 2021

ABSTRACT

Melting relations in the $MgSiO_3$–SiO_2 system have been investigated at 13.5 GPa using a Kawai-type multianvil apparatus. The system displays eutectic melting with the eutectic point located at $SiO_2/(SiO_2+MgO)$ = 0.61 (in mol; which is denoted by X_{Si} hereafter) and at 2350 ± 50 °C. Taking into account the eutectic compositions at lower pressures shown in previous studies, i.e., 0.556 at 1 GPa (Hudon et al., 2005) and 0.60 at 5 GPa (Dalton and Presnall, 1997), the eutectic composition is slightly enriched in SiO_2 with increasing pressure. The silica-rich eutectic composition is not consistent with the present peridotitic mantle composition (X_{Si} = 0.43). Considering Si incorporation into iron alloys in a magma ocean, however, mass-balance calculations based on an E-chondrite model demonstrate that the silicate magma ocean could have X_{Si} consistent with the present peridotitic mantle.

Keywords: Melting; High pressure; $MgSiO_3$–SiO_2 system; Mantle; Enstatite chondrite model; Multianvil; Pressure calibration; Thermal expansion

INTRODUCTION

Understanding the melting behavior of silicates is essential for modeling the chemical differentiation in a deep magma ocean in the early stages of Earth's history. Therefore, melting relations in the MgO–SiO_2 system as a representative of the mantle have been extensively studied since the pioneering work by Bowen and Anderson (1914). Furthermore, many scenarios of chemical differentiation in a magma ocean have been proposed based on the results of high-pressure melting experiments (e.g., Kato and Kumazawa, 1985; Presnall and Gasparik, 1990; Ito and Katsura, 1992; Presnall et al., 1998). However, almost all of these works have been carried out on bulk compositions ranging from MgO to $MgSiO_3$, assuming that the bulk mantle composition is peridotitic or close to that derived from CI chondrites (e.g., Ringwood, 1966; Jagoutz et al., 1979; Takahashi, 1986; McDonough and Sun, 1995). Because the chemical compositions of CI chondrites are close to the composition of the solar composition, the bulk composition of the Earth is considered to be similar to that of CI chondrites. (e.g., Anders and Grevesse, 1989; Allègre et al., 1995). However, the isotope compositions cannot be explained by the CI chondrite model. Highly precise isotope analyses (O, N, Mo, Ru, Os, Cr, and Ti) show that the Earth, Moon, and enstatite chondrites (E-chondrites) have almost indistinguishable isotopic compositions (e.g., Qin et al., 2010; Javoy et al., 2010; Warren, 2011; Dauphas and Schauble, 2016). Therefore, the E-chondrite model has been postulated as a viable the Earth composition model (e.g., Javoy et al., 2010; Dauphas, 2017; Piani et al., 2020). Contrary to the similar isotope compositions between E-chondrites and the Earth, the X_{Si} (= SiO_2/(SiO_2+MgO) (in mol)) of E-chondrites (0.53 to 0.58; Wasson and Kallemeyn, 1988) is substantially higher than that of peridotitic mantle

(0.43; Takahashi, 1986). This has been argued as one of the major obstacles to the E-chondrite model (e.g., Fitoussi and Bourdon, 2012).

To understand mantle differentiation in the E-chondrite model and to evaluate the model, it is indispensable to clarify the melting relations in the $MgSiO_3$–SiO_2 system at high pressures. Nevertheless, there have been limited studies on the melting behavior of the $MgSiO_3$–SiO_2 system at high pressures: e.g., at 1 GPa using the piston cylinder (Hudon et al., 2005) and at 5 GPa using the Kawai-type multianvil apparatus (KMAA) (Dalton and Presnall, 1997). On the other hand, using a diamond anvil cell (DAC), melting experiments in the MgO–SiO_2 system were carried out up to 139 GPa (Baron et al., 2017; Ozawa et al., 2018). According to these studies, the $MgSiO_3$–SiO_2 system displays eutectic melting and the X_{Si} of the eutectic compositions systematically increases with increased pressure.

In comparison with the DAC, the KMAA has remarkable advantages in investigating the high-pressure phase equilibria of silicates because a much larger sample volume is available under stable temperature conditions (e.g., Ito et al., 2007, Xie et al., 2020). In this study, we determine the melting relations in the $MgSiO_3$–SiO_2 system at 13.5 GPa as precisely as possible using the KMAA. In addition, we evaluate the E-chondrite model based on the melting relations in the $MgSiO_3$–SiO_2 system determined in the present study combined with those determined in previous studies.

In a multianvil apparatus, the sample pressure can be substantially altered upon heating due to the thermal expansion and the mechanical weakening of the pressure medium. As shown in previous studies conducted at high temperatures (e.g., Ito and Takahashi, 1989; Fei et al., 2004; Leinenweber et al., 2012), the effects of temperature at > 1000 °C on the generated pressure are not negligible. In this study, the sample heating

was conducted from 2250 to around 3000 °C. Therefore, we also evaluate the effects of the generated pressure at such high temperatures.

EXPERIMENTAL METHODS

Seven starting materials with X_{Si} = 0.55, 0.60, 0.61, 0.70, 0.80, 0.90, and 1.00 were prepared (Table 1). The starting materials were prepared by mixing synthetic enstatite glass with high purity SiO_2 glass (Kojundo Chemical Laboratory, Japan, 99.999% purity) by weighing in the prescribed proportions. The glasses were weighed to have the prescribed compositions. Subsequently, they were mixed and ground using an alumina ceramic mortar to achieve homogeneity, and the grain size was less than 3 μm.

High-pressure and high-temperature experiments at 13.5 GPa and up to ca. 3000 °C were undertaken using the KMAA, USSA-1000, installed at the Institute for Planetary Materials, Okayama University. Tungsten carbide (WC) cubes with a 32 mm edge length and 4 mm truncated edge were employed as the second anvil. The specimen configuration is schematically illustrated in Fig. 1, similar to that employed by Ito and Katsura (1992). Octahedral pressure media were made of magnesia +5% Cr_2O_3 with a 10 mm edge length. The powdered sample was directly loaded into a cylindrical rhenium heater placed inside a lanthanum chromite sleeve for thermal insulation. The sample temperature was monitored by a W25Re/W3Re thermocouple. The thermocouple junction was located at the midpoint of the Re-cylindrical heater (Fig. 1). To remove moisture, the octahedral pressure medium was heated at 1000 °C for 1 h. The whole assembly was dried at 200 °C for 1 h immediately before compression in every experimental run. No correction was made for the pressure effect on the emf of the

thermocouple. The pressure calibration was carried out at 2500 and 2850 °C based on the coesite–stishovite transition in SiO_2 determined by Zhang et al. (1996).

First, the sample was compressed to 13.5 GPa at room temperature and then heated to the prescribed temperature at a rate of 100 °C/min. The sample was kept at the prescribed temperature for 5 min and was subsequently quenched by shutting off the electric power supply. Pressure was released at a rate of about 3 GPa/h. In Fig. 2, examples of the thermocouple temperature are plotted against the input power for typical runs. The relation between the temperature and the input power can be approximated by a quadratic relationship. When the thermocouple was accidentally broken during heating, the temperature was estimated by extrapolating the quadratic relationship obtained until just before thermocouple breakdown. The heating temperature was controlled to ± 20 °C at peak temperature in each experimental run. In the case that the thermocouple was broken, the uncertainties in temperature determination are estimated to be ± 50 °C at ≤2500 °C and ± 120 °C at >2500 °C based on the differences between the measured temperature and the estimated temperature using the fitting curve which were observed when the thermocouple survived.

The recovered run product was mounted on glass with the longitudinal axis of the heater and the thermocouple wires parallel to the glass surface, and the product was subsequently embedded in epoxy resin. Afterward, the run product was ground and polished until the surface of the central region of the sample appeared together with the thermocouple.

To observe the variation of phases along the temperature gradient through the sample, run products were observed using a field-emission scanning electron microscope

(FE-SEM: JEOL JSM-7001F) with an acceleration voltage and probe current of 15 kV and 15 nA, respectively.

Phases in the run products were identified by micro-focused X-ray diffractometry (MF-XRD: Rigaku RINT RAPID II – CMF) with a Cu source. The applied voltage and the current were 40 kV and 30 mA, respectively. The detector was a curved imaging plate detector (camera length: 127.30 mm).

The chemical compositions of the quenched glasses and solids present in the run products were determined using an electron probe microanalyzer (EPMA: JEOL JXA-8800). In both the quantitative analysis and the elemental mapping, the accelerating voltage and the beam current were 15 kV and 12 nA, respectively. For quantitative analysis, the spot sizes were ≤10 μm with the standards of MgO and $CaSiO_3$/SiO_2 for Mg and Si, respectively. The analytical uncertainty was less than 0.7% (2σ) in X_{Si}. For elemental mapping, the beam size was 2 μm.

RESULTS AND DISCUSSION

Pressure calibration

The generated pressure was assessed to be 13.5 GPa based on the pressure calibration described below. The pressure calibration was based on the phase relations of coesite–stishovite determined from the in situ X-ray diffraction observations by Zhang et al. (1996) in which the dP/dT slope of the coesite–stishovite phase boundary was determined at 500–1530 °C, given by the following equation:

$$P\ (\text{GPa}) = 6.1(4) + 0.0026(2)\ T\ (^\circ\text{C}) \qquad (1).$$

As described in Zhang et al. (1996), the estimated pressure of the coesite–stishovite–liquid triple point was 13.3 GPa, obtained by assuming a linear extrapolation of the slope

155 to the melting temperature of coesite and stishovite (2800 °C) determined by Zhang et al.
156 (1993) in which the phase boundary was determined from quench experimental studies.
157 The estimated pressure (13.3 GPa in Zhang et al., 1996) is close to the 13.7 GPa at
158 2800 °C reported in the study by Zhang et al. (1993). Based on the adequate consistency,
159 the *dP/dT* slope of the phase boundary of coesite–stishovite determined by Zhang et al.
160 (1996) was extrapolated linearly for the pressure calibration in the present study
161 conducted at ≥2250 °C.

162 Using high purity quartz glass (99.999%) as a starting material in the present
163 study, the coesite–stishovite transition temperature was investigated at 2.4 MN. As shown
164 in the results of experiments 1K3204 and 1K3207 (Table 1), the analyses of these run
165 products by MF-XRD indicated that the phases of SiO_2 were stishovite and coesite at
166 2800 and 2900 °C, respectively, at the central high-temperature region in the run products.
167 Based on these results and the following discussion, it is concluded that 2850 °C is the
168 transition temperature of coesite–stishovite at 2.4 MN in the present study. Using
169 Equation 1, the transition pressure of the coesite–stishovite transition at 2850 °C was 13.5
170 ± 1.3 GPa, at a press load of 2.4 MN. The uncertainty was estimated from the uncertainties
171 in both of Equation 1 and the temperature determination in this study. Zhang et al. (1993)
172 showed that the melting temperature of coesite did not change much (2750 to 2800 °C)
173 when the pressure increased from 11 to 13.7 GPa. The transition temperature determined
174 in the present study is slightly higher than the melting temperature of coesite determined
175 by Zhang et al. (1993). Considering the uncertainties in the determinations of temperature
176 in Zhang et al. (1993) and the present study, ± 50 °C and ± 120 °C, respectively, Equation
177 1 can be extrapolated to 2850 °C to determine the generated pressure in the present study.

178 At room temperature, the pressure calibration was made by detecting abrupt
179 changes in electrical resistance associated with the following phase transitions: Bi I–II
180 (2.55 GPa), Bi III–V (7.7 GPa), metallic transitions in GaAs (18.2 GPa) and GaP (23
181 GPa). Compared with the sample pressure, 10.5 GPa, which corresponds to 2.4 MN
182 calibrated at room temperature, the generated pressure (13.5 GPa) at 2850 ℃ is 3.0 GPa
183 higher (Fig. 3).

184 We conducted a further investigation to evaluate the difference in pressure
185 calibration between room temperature and another high temperature, 2500 ℃. In this
186 investigation, seven samples (high purity quartz glass, 99.999%) were compressed at the
187 following press load conditions, 1.6, 2.0, 2.2, 2.3, 2,4, 2.8, and 3.2 MN and heated at
188 2500 ℃. In the run products recovered from ≥2.3 MN, stishovite was observed at the
189 central high-temperature region. In the run products compressed at ≤2.2 MN, coesite was
190 observed at the central high-temperature region. These results indicate that the coesite–
191 stishovite transition occurs between 2.2 and 2.3 MN at 2500 ℃. It is concluded, therefore,
192 that the press load of coesite–stishovite transition is 2.25 MN (mean of 2.2 and 2.3 MN)
193 at 2500 ℃. Based on Equation 1, the generated pressure was calculated to be 12.6 ± 1.0
194 GPa, which corresponds to a press load of 2.25 MN at 2500 ℃, indicating that the sample
195 pressure is 2.7 GPa higher than that determined at room temperature (Fig. 3).

196 The evaluation of the effect of temperature on the sample pressure has been
197 undertaken in previous studies (e.g., Gasparik, 1989; Ito and Takahashi, 1989). Based on
198 the results of pressure calibration carried out at room temperature, 1000 and 1600 ℃, Ito
199 and Takahashi (1989) suggested that the differences observed in calibration curves at each
200 temperature were due to the transformation effect of the constituents in the experimental
201 cell assembly accompanied by volume contraction (e.g., the zirconia sleeve for an

insulator in their study) and due to the thermal expansion of the assembly, which was pronounced at higher temperature. In the present study, the increase of sample pressures can be dominantly caused by thermal pressure due to expansion of the cell assembly at high temperature. The observed increases in generated pressure were 2.7 GPa at 2.25 MN and 2500 ℃, and 3.0 GPa at 2.4 MN and 2850 ℃ (Fig. 3).

The maximum temperature in the present study was 2900 ℃, quite close to 2850 ℃ at which the pressure calibration was conducted at 2.4 MN. Therefore, we concluded that the press load at 2.4 MN corresponds to the generated pressure of 13.5 GPa also at 2900 ℃. On the other hand, the minimum temperature (2250 ℃) is 250 ℃ lower than 2500 ℃ at which the above-mentioned experiments were conducted. The difference of the generated pressures between room temperature and 2500 ℃ was 2.7 GPa at 2.25 MN. Thus, we assumed that the difference of 2.7 GPa was maintained at 2.4 MN at 2500 ℃. If so, the generated pressure corresponding to a press load of 2.4 MN at 2500 ℃ is estimated to be 13.2 GPa because 10.5 GPa corresponds to 2.4 MN calibrated at room temperature. Consequently, the difference of the generated pressure between 2500 and 2850 ℃ (350 ℃ difference) is 0.3 GPa (= 13.5 – 13.2 GPa). The temperature difference between the minimum temperature (2250 ℃) and 2500 ℃ is 250 ℃, smaller than the difference of 350 ℃ between 2500 and 2850 ℃. Therefore, we assumed that the difference in the generated pressures between 2250 and 2500 ℃ at 2.4 MN was less than 0.3 GPa. At 2250 ℃, the uncertainty in the determination of the generated pressure using Equation 1 was estimated to be +0.9/-1.0 GPa. Considering those uncertainties in the determination of the generated pressure at 2250, 2500 and 2850 ℃ with the differences in the generated pressures at those temperatures, it is concluded that the generated

pressure corresponds to 13.5 GPa at the press load of 2.4 MN at temperatures ranging from 2250 to 2900 ℃ in the present study.

Observation of the run products

The experimental results are summarized in Table 1 together with the experimental conditions, observed phases at the central high-temperature region in each run product, the X_{Si} values of liquid coexisting with liquidus phases, and that of the liquidus phase. Observations in various compositions were as follows.

Starting material compositions: $X_{Si} \leq 0.61$

Sample 1K2987 (X_{Si} = 0.61) was heated at 2500 ℃. Figure 4 is a Si image map of the cross section of run product 1K2987 from the center (the highest *T* region) to the end (the lowest *T* region). At the low-temperature side, an arched Si-rich zone was observed that contained stishovite and liquid. At the further low-temperature side, stishovite and enstatite were observed. In the area from the center to the Si-rich zone, quenched textures were observed, indicating that the area corresponded to the liquid and that the liquidus temperature was lower than 2500 ℃ at X_{Si} = 0.61. These observations indicate that the liquidus corresponds to the boundary between the quenched liquid and the Si-rich zone. The solidus corresponds to the margin at the low-temperature side in the Si-rich arched zone. Based on these results, it was demonstrated that the liquidus phase was stishovite at X_{Si} = 0.61.

In the run products of samples 1K3105 (X_{Si} = 0.55) and 1K3138 (X_{Si} = 0.60) heated at 2400 ℃, melting textures were observed at the central high-temperature regions. These results indicate that these samples were above the liquidus temperature at 2400 ℃.

In other words, the liquidus temperature should be below 2400 °C between X_{Si} = 0.55 and X_{Si} = 0.60. In these samples, enstatites crystalized along the margin of the liquid region located at the low-temperature side in each run product as shown in Fig. 5. These results indicate that the liquidus phase is enstatite in the compositions of $X_{Si} \leq 0.60$, contrasting to 1K2987 (X_{Si} = 0.61) where the liquidus phase was stishovite. The observed liquidus phases in 1K2987 and 1K3138 strictly constrain the location of the eutectic point between X_{Si} = 0.60 and X_{Si} = 0.61, and we propose that the eutectic composition is X_{Si} = 0.61 (see Fig. 8).

Run products of 1K3024 and 1K3074 (X_{Si} = 0.55), heated at 2250 and 2300 °C, respectively, did not show any molten texture even around the central high-temperature region of the samples. These results indicate that the solidus temperature is higher than 2300 °C.

Starting material compositions: $X_{Si} \geq 0.70$

Sample 1K3002 (X_{Si} = 0.70) was heated at 2500 °C. In the run product, large euhedral stishovite crystals (>50 μm) were observed in the molten portion around the central high-temperature region (Fig. 6). This feature indicates the coexistence of liquid and stishovite. The composition of the liquid was determined to be X_{Si} = 0.60, almost identical to the bulk composition of 1K2987 (X_{Si} = 0.61) that showed molten texture at 2500 °C.

In the sample 1K3129 (X_{Si} = 0.70), heated at 2700 °C, there was a tiny amount of stishovite crystals coexisting with the liquid at the central high-temperature region. This observation indicates that the sample was in solid–liquid coexistence at 2700 °C.

The X_{Si} of this liquid was 0.69, which was slightly less than the starting composition (X_{Si} = 0.70).

Sample 1K3157 (X_{Si} = 0.80) was heated at 2800 °C. In the high-temperature region of the run product, large crystals (>5 μm) of stishovite were formed in aggregates of fine particles (<1 μm) (Fig. 7). The average composition of the aggregate was X_{Si} = 0.72, showing a reduction of the SiO_2 component from the starting composition, X_{Si} = 0.80. Based on these results, the sample was in solid–liquid coexistence at 2800 °C.

During heating of sample 1K3178 (X_{Si} = 0.90), the heater was broken at ~2900 °C. In the recovered run product, we observed that both the Re-capsule and $LaCrO_3$-insulator were molten and that the molten part of the sample was extensively contaminated with Re, La, and Cr from the heater and the insulator around the central high-temperature region. These results indicate that the actual temperature on heating might be over the melting temperature of Re, i.e., 3180 °C (at atmosphere). The mixing of sample and contaminants (Re, La, and Cr) indicates that the sample was heated over the liquidus temperature. It is concluded, therefore, that a conceivable minimum liquidus temperature would be 2900 °C for X_{Si} = 0.90.

As mentioned in the previous section, samples 1K3204 and 1K3207 (X_{Si} = 1.00) were heated at 2800 and 2900 °C, respectively. In the central high-temperature region of the run products, the phases in 1K3204 and 1K3212 were stishovite and coesite, respectively. As mentioned, the liquidus phase observed in samples 1K3002 (X_{Si} = 0.70, heated at 2500 °C) and 1K3157 (X_{Si} = 0.80, heated at 2800 °C) was stishovite. These results provide supporting evidence that the temperature of the coesite–stishovite transition is higher than 2800 °C at 13.5 GPa. Based on these results, the temperature of

the phase transition between those two phases is around 2850 ℃ as a mean value of 2800 and 2900 ℃.

Phase relations in the $MgSiO_3$–SiO_2 system at 13.5 GPa

We summarize the experimental results obtained in the present study in the binary eutectic melting phase diagram in Fig. 8.

The results of 1K3024, 1K3074, and 1K3105 (X_{Si} = 0.55), heated at 2250, 2300, and 2400 ℃, respectively, indicate that the solidus temperature is between 2300 and 2400 ℃. Taking into consideration the uncertainty in the determination of temperature, we conclude that the solidus temperature is 2350 ℃ as the averaged value of 2300 and 2400 ℃, which is also the eutectic temperature at X_{Si} = 0.61, as shown in Fig. 8. Hudon et al. (2005) showed two eutectic points at 1 GPa, X_{Si} = 0.556 and 0.969 in the $MgSiO_3$–SiO_2 system. At 5 GPa, Dalton and Presnall (1997) showed that the two-liquid field (miscibility gap) disappeared completely, resulting in one eutectic point, X_{Si} = 0.60. Focused on the eutectic points located at the $MgSiO_3$-rich side, the eutectic composition becomes slightly enriched in SiO_2 with increasing pressure.

The results of 1K3105 (X_{Si} = 0.55) indicate that the temperature of 2400 ℃ was above the liquidus at X_{Si} = 0.55. That is, the liquidus should be located between 2350 and 2400 ℃. Combined with these results and the eutectic point, X_{Si} = 0.61 at 2350 ℃, the melting point of enstatite is likely to be 2400 ℃. The liquidus curve of enstatite determined by Presnall and Gasparik (1990) showed that the melting temperature of enstatite was 2295 ℃ at 13.5 GPa. Thus, taking into account the uncertainties in temperature and pressure in the present study (± 50 ℃ at 2500 ℃ or less) and in Presnall

and Gasparik (1990) (± 30 °C), the melting temperature of enstatite in the present study is generally consistent with that in Presnall and Gasparik (1990).

Based on experimental results of the compositions of liquid (X_{Si}) in solid–liquid coexistence and heating temperatures of 1K3002, 1K3129, and 1K3157 (Table 1), the liquidus curve was drawn between X_{Si} = 0.61 and 0.80 (Fig. 8).

The results of 1K3204 and 1K3207 (X_{Si} = 1.00) indicate that the melting temperature of coesite is higher than 2900 °C at 13.5 GPa. Zhang et al. (1993) showed that the melting temperature of coesite slightly changed from 2750 to 2800 °C as the pressure increased from 11 to 13.7 GPa at which the coesite–stishovite–liquid triple point is located. The inconsistency between the results in the present study and those in Zhang et al. (1993) can be attributed to the uncertainty in determining the temperature and pressure in both studies. Taking into account the uncertainty of temperature and pressure (± 120 °C at >2500 °C in the present study and ± 50 °C at >2300 °C in Zhang et al. (1993) for temperature; ± 1.0 GPa in the present study and unclear in Zhang et al. (1993) for pressure), it is concluded that the melting temperature of coesite is around 2950 °C in the present study. When also taking into consideration the results of 1K3178 that indicate the liquidus temperature at 0.90 of X_{Si} was lower than 3180 °C, the liquidus curve was extrapolated from 0.70 to 1.00 of X_{Si}, as shown in Fig. 8.

IMPLICATIONS

A terrestrial magma ocean played an important role in differentiating the mantle in the early stages of the Earth (e.g., Ringwood, 1975). According to numerical models, the depth of the magma ocean was greater than 1000 km (e.g., Hayashi et al., 1979; Kaula, 1979). The abundance of siderophile elements in the mantle provides constraints on

magma ocean depth, approximately 700–1200 km (e.g., Li and Agee, 1996; Righter et al., 1997). As mentioned, the pressure dependency of the eutectic compositions in the $MgSiO_3$–SiO_2 system is quite small. The X_{Si} value of the eutectic composition increases from 0.556 to 0.61 in a range from 1 to 13.5 GPa (down to ~400 km depth in the mantle) (Dalton and Presnall, 1997; Hudon et al., 2005; this study), which are close to those of E-chondrites (0.533–0.577; Wasson and Kallemeyn, 1988). Using a DAC, experimentally determined eutectic compositions (X_{Si}) at 41, 128, and 139 GPa were 0.60, 0.66, and 0.66, respectively (Ozawa et al., 2018). Combined with all the available experimentally determined eutectic compositions, the X_{Si} increases significantly to ~0.61 with increased pressure when lower than 50 GPa and then increases asymptotically to 0.66 up to 128 GPa (Fig. 9). Without consideration of Si incorporation into metals during core formation, those eutectic compositions indicate that the compositions of the melts produced from E-chondrite source materials are around 0.6, which is significantly higher than the estimate of the current upper mantle, 0.43.

It is well known that Si becomes more siderophile with increasing temperature and pressure and with decreasing oxygen fugacity (e.g., Kilburn and Wood, 1997; Wade and Wood, 2005). Since Birch (1952) proposed that the Earth's core contained ~10 wt.% light elements in iron and nickel alloy ("the core density deficit"), investigations on the incorporations of light elements such as Si, O, S, C and H to the core have been vigorously conducted. The Si content in the core is controversial and is proposed to be in the range of 2.8–14 wt.% (see the review articles, e.g., Hirose et al., 2013; Li and Fei, 2014). Using *ab initio* molecular dynamics to calculate the density and bulk sound velocity in liquid metal alloys at the pressure and temperature conditions of Earth's outer core, Badro et al. (2014) suggested that Si concentration in the core cannot be higher than 4.5 wt.%.

366 Recently, Umemoto and Hirose (2020) suggested that the existence of H in the core was
367 not negligible and could allow liquid iron with ~9–11 wt.% Si, which was compatible
368 with observations examining the density and bulk sound velocity of Earth's outer core by
369 comparing first-principles calculations on binary liquid iron alloys containing Si, O, S, C,
370 and H with the PREM model (Dziewonski and Anderson, 1981). On the other hand,
371 through determining the P wave velocity of liquid Fe–Si at the core–mantle boundary
372 conditions based on inelastic X-ray scattering measurements in a laser-heated DAC,
373 Nakajima et al. (2020) found the upper limit of silicon concentration in the outer core to
374 be <1.9 wt.%. This value is too small to explain the core density deficit. In addition, recent
375 core formation models based on metal-silicate element partitioning predicted that 2 to 9
376 wt.% Si may have been incorporated into core metals in a deep magma ocean (Rubie et
377 al., 2011; Siebert et al., 2013; Wood et al., 2009). Therefore, Nakajima et al. (2020)
378 suggested that the present-day liquid outer core was depleted in silicon after crystallizing
379 SiO_2 (and $MgSiO_3$) through the history of the Earth.

380 To evaluate the E-chondrite model, taking into account the incorporation of Si
381 into the core during core formation in a magma ocean, we estimated the range of Si
382 content in the core assuming an E-chondrite model and evaluated the range in comparison
383 to the Si contents in the core proposed in previous works. In the estimation of the Si
384 contents in the core using an E-chondrite model, we investigated the conditions of the
385 depth of magma ocean and the Si content in the core when the Xsi of the silicate melt in
386 a magma ocean was same as that of peridotitic mantle. In the calculations of the Xsi of
387 the silicate melt in a magma ocean before and after the core segregation, we considered
388 the following two melting conditions: (a) eutectic melting and (b) complete melting. In
389 case (a), the X_{Si} of the silicate melts before incorporation of Si is the eutectic composition

which changes with the depth in the magma ocean. The temperatures of the magma ocean are the eutectic temperatures in the $MgSiO_3$–SiO_2 system, which also change with depth in the magma ocean and which are the lowest in the possible melting temperatures. In case (b), the temperatures of the magma ocean are over the liquidus temperatures. The X_{Si} of the silicate melts before incorporation of Si is same as that of the original material, enstatite chondrite. In the calculations, we also assumed a single-stage process for the magma ocean model whose depth was 700 to 1200 km (e.g., Li and Agee, 1996; Righter et al., 1997). The details in the calculations are shown in Supplementary materials.

Figure S1 shows the relations between the compositions of the silicate melt (X_{Si}) after core segregation for the following cases of Si contents in the core, 1.9, 2.7, 4.0 and 8.8 wt.% in case (a), and 1.9, 5.0, 8.8 and 10.0 wt.% in case (b). In case (a), the silicate melt composition after core segregation (X_{Si}) is that of peridotitic mantle composition (X_{Si} = 0.43) when the content of Si in the core is 2.7 wt.% and the depth of magma ocean is 700 km (Fig. S1a). Moreover, when the content of Si in the core is 4.0 wt.% and the depth of magma ocean is 1200 km, the X_{Si} of the silicate melt after the core segregation is also 0.43 (Fig. S1a). In other words, if the original material of the Earth is E-chondrite, the Si content in the core is estimated to be 2.7 to 4.0 wt.% in the eutectic melting model. On the other hand, Fig. S1b indicates that estimated Si contents in the core are 5.0 to 8.6 wt.% in case (b), which are higher than those obtained in case (a). The actual temperature of the magma ocean would be between the cases of (a) and (b). Therefore, those calculations indicate that Si content in the core would be between 2.7 to 8.6 wt.%, which is within the range of 2 to 9 wt.% Si in the core as predicted by metal-silicate element partitioning. Our results indicate that the E-chondrite model may explain the bulk Earth composition if the

413 Si depletion in the core proposed by Nakajima et al. (2020) has operated through Earth's
414 history.
415

Acknowledgment

We acknowledge S. Yamashita and M. Akaogi for their fruitful discussions and comments. We also acknowledge T. Yoshino, D. Yamazaki, N. Tsujino, and M. Kanzaki for their helpful comments and technical support in experiments. We are deeply grateful to M. R. M. Izawa for his constructive comments and for improving the text. Insightful comments by two reviewers, M. Walter and J. Li, were helpful in improving the manuscript, and we are thankful to M. Walter for greatly improving the text. We appreciate S. Tateno for his helpful comments to give us a catalyst for advancing this study. We thank L. Xie, F. Xu, and C. Oka for their technical support.

REFERENCES CITED

Anderson, D.L. and Kovach R.L. (1967) The composition of the terrestrial planets. Earth and Planetary Science Letters, 3, 19–24.

Badro, J., Côté, A.S., and Brodholt, J.P. (2014) A seismologically consistent compositional model of Earth's core. Proceedings of the National Academy of Sciences of the United States of America, 111, 7542-7545.

Baron, M.A., Lord, O.T., Myhill, R., Thomson, A.R., Wang, W., Trønnes, R.G., and Walter, M.J. (2017) Experimental constraints on melting temperatures in the MgO–SiO2 system at lower mantle pressures. Earth and Planetary Science Letters, 472, 186–196.

Birch, F. (1952) Elasticity and constitution of the Earth's interior. Journal of Geophysical Research, 57, 227–286.

Birck, J., Rotaru, M,. and Allègre, C. (1999) ^{53}Mn–^{53}Cr evolution of the solar system. Geochimica et Cosmochimica Acta, 63, 4111–4117.

Bowen, N.L. and Anderson, O. (1914) The binary system MgO – SiO_2. American Journal of Science, 4th ser. 37, 487–500.

Cartigny, P., Boyd, S.R., Harris, J., and Javoy, M. (1997) Nitrogen isotopes in peridotitic diamonds from China: the mantle signature. Terra Nova 94, 175–179.

Clayton, R., Mayeda, T., and Rubin, A.E. (1984) Oxygen isotope composition of enstatite chondrites and aubrites. Journal of Geophysical Research, 89, C245–C249.

Dahl, T.W. and Stevenson, D.J. (2010) Turbulent mixing of metal and silicate during planet accretion — And interpretation of the Hf–W chronometer. Earth and Planetary Science Letters, 295, 177–186.

449 Dalton, J.A. and Presnall, D.C. (1997) No liquid immiscibility in the system $MgSiO_3$-
450 SiO_2 at 5.0 GPa. Geochimica et Cosmochimica Acta, 61, 2367–2373.
451 Dauphas, N., Davis, A.M., Marty, B., and Reisberg, L. (2004) The cosmic molybdenum-
452 ruthenium isotope correlation. Earth and Planetary Science Letters, 226, 465–
453 475.
454 Fei, Y., Li, J., Hirose, K., Minarik, W., Ormana, J.V., Sanloup, C., van Westrenen, W.,
455 Komabayashi, T., and Funakoshi, K. (2004) A critical evaluation of pressure
456 scales at high temperatures by in situ X-ray diffraction measurements. Physics
457 of the Earth and Planetary Interiors, 143–144, 515–526.
458 Gasparik, T. (1989) Transformation of enstatite – dioside – jadite pyroxenes to garnet.
459 Contributions to Mineralogy and Petrology, 102, 389–405.
460 Hayashi, C., Nakazawa, K., and Mizuno, H. (1979) Earth's melting due to the blanketing
461 effect of the primordial dense atmosphere. Earth and Planetary Science Letters,
462 43, 22–28.
463 Hirose, K., Labrosse, S., and Hernlund, J. (2013) Composition and state of the core. Annu.
464 Annual Review of Earth and Planetary Sciences, 41, 657–691.
465 Hudon, P., Jung, I., and Baker, D. (2005). Experimental investigation and optimization
466 of thermodynamic properties and phase diagrams in the systems CaO-SiO_2,
467 MgO-SiO_2, $CaMgSi_2O_6$-SiO_2 and $CaMgSi_2O_6$-Mg_2SiO_4 to 1.0 GPa. Journal of
468 Petrology, 46, 1859–1880.
469 Ito, E. and Katsura T. (1992) Melting of ferromagnesian silicates under the lower mantle
470 conditions. American Geophysical Union, Geophysical Monograph Series, 67,
471 315–322.

Ito, E. (2007) Theory and practice — multianvil cells and high-pressure experimental methods. In: G.D. Price and G. Schubert, Ed., Treatises on Geophysics. 2nd edition, p. 197-230. Elsevier B.V., Oxford.

Ito, E. and Takahashi, E. (1989) Postspinel transformation in the system Mg_2SiO_4-Fe_2SiO_4 and some geophysical implications. Journal of Geophysical Research, 94, 10637–10646.

Jagoutz, E., Palme, H., Baddenhausen, H., Blum, K., Cendales, M., Dreibus, G., Spettel, B., Lorenz, V., and Wänke, H. (1979) The abundances of major, minor and trace elements in the Earth's mantle as derived from primitive ultramafic nodules. Proc. Lunar and Planetary Science Conference, 10th, 2031–2050.

Javoy, M., Kaminski, M., Guyot, F., Andrault, D., Sanloup, C., Moreira, M., Labrosse, S., Jambon, A., Agrinier, P., Davaille, A., and Jaupart, C. (2010) The chemical composition of the Earth: Enstatite chondrite models. Earth and Planetary Science Letters, 293, 259–268.

Kato, T. and Kumazawa M. (1985) Effect of high pressure on the melting relation in the system Mg_2SiO_4 - $MgSiO_3$ Part I. Eutectic relation up to 7 GPa. Journal of Physics of the Earth, 33, 513–524.

Kaula, W.M. (1979) Thermal evolution of the Earth and moon growing by planetesimal impacts. Journal of Geophysical Research, 84, 999–1008.

Kilburn M.R. and Wood B.J. (1997) Metal-silicate partitioning and the incompatibility of S and Si during core formation. Earth and Planetary Science Letters, 152, 139–148.

Leinenweber, K.D., Tyburczy, J.A., Sharp, T.G., Soignard, E., Diedrich, T., Petuskey, T.D., Wang, Y., and Mosenfelder, J.L. (2012) Cell assemblies for reproducible

multi-anvil experiments (the COMPRES assemblies) American Mineralogist, 97, 353–368.

Li, J. and Agee, C.B. (1996) Geochemistry of mantle–core differentiation at high pressure. Nature, 381, 686–689.

Li, J. and Fei, Y. (2014) Experimental constraints on core composition. In: Holland, H.D., Turekian, K.K. (Eds.), Treatise on Geochemistry, vol. 3, second ed. Elsevier, Amsterdam, pp. 527–557.

McDonough, W.F. and Sun, S. (1995) The composition of the Earth. Chemical Geology, 120, 223–253.

Meisel, R., Walker, R., and Morgan, J. (1996) The osmium isotopic composition of the Earth's primitive upper mantle. Nature, 383, 517–520.

Nakajima, Y., Kawaguchi, S.I., Hirose, K., Tateno, S., Kuwayama, Y., Sinmyo, R., Ozawa, H., Tsutsui, S., Uchiyama, H., and Baron, A.Q. (2020) Silicon-depleted present-day Earth's outer core revealed by sound velocity measurements of liquid Fe-Si alloy. Journal of Geophysical Research, Solid Earth 125(6). DOI: 10.1029/2020JB019399.

Ozawa, K., Anzai, M., Hirose, K., Shinmyo, R., and Tateno, S. (2018) Experimental determination of eutectic liquid compositions in the MgO-SiO_2 system to the lowermost mantle pressures. Geophysical Research Letters, DOI: 10.1029/2018GL079313.

Piani, L., Marrocchi, Y., Rigaudier, T., Vacher, L.G., Thomassin, D., and Marty, B. (2020) Earth's water may have been inherited from material similar to enstatite chondrite meteorites. Science, 369, 1110–1113.

519 Poirier J.-P. (2000) Introduction to the physics of the Earth's interior, 2nd. ed. Cambridge
520 University Press, Cambridge, pp. 312.
521 Presnall, D.C. and Gasparic, T. (1990) Melting of enstatite ($MgSiO_3$) from 10 to 16.5 GPa
522 and the forsterite (Mg_2SiO_4) - majorite ($MgSiO_3$) eutectic at 16.5 GPa:
523 Implications for the origin of the mantle. Journal of Geophysical Research, 95,
524 15771–15777.
525 Presnall, D.C., Weng, Yi-H., Milholland, C.S., and Walter, M.J. (1998) Liquidus phase
526 relations in the system MgO-$MgSiO_3$ at pressures up to 25 GPa — constraints
527 on crystallization of a molten Hadean mantle. Physics of the Earth and Planetary
528 Interiors, 107, 83–95.
529 Righter, K., Drake, M.J., and Yaxley, G. (1997) Prediction of siderophile element metal–
530 silicate partition coefficients to 20 GPa and 2800 °C: the effects of pressure,
531 temperature, oxygen fugacity, and silicate and metallic melt compositions.
532 Physics of the Earth and Planetary Interiors, 100, 115–134.
533 Ringwood. A.E. (1966) The chemical composition and origin of the Earth. In: Hurley,
534 P.M. (Ed.). Advances in Earth Sciences. MIT Press, Cambridge, Mass. pp. 287–
535 356.
536 Ringwood, A.E. (1975) Composition and petrology of the Earth's mantle. McGraw-Hill,
537 New York, 618 pp.
538 Righter, K., Drake, M.J., and Yaxley, G. (1997) Prediction of siderophile element metal-
539 silicate partition coefficients to 20GPa and 2800ºC: the effects of pressure,
540 temperature, oxygen fugacity, and silicate and metallic melt compositions.
541 Physics of the Earth and Planetary Interiors, 100, 115–134.

Rubie, D.C., Frost, D.J., Mann, U., Asahara, Y., Nimmo, F., Tsuno, K., Kegler, P.,Holzheid, A., and Palme, H. (2011). Heterogeneous accretion, composition and core-mantle differentiation of the Earth. Earth and Planetary Science Letters, 301, 31–42.

Rubie, D.C., Jacobson, S.A., Morbidelli, A., O'Brien, D.P., Young, E.D., de Vries, J., Nimmo, F., Palme, H., and Frost, D.J. (2015) Accretion and differentiation of the terrestrial planets with implications for the compositions of early-formed Solar System bodies and accretion of water. Icarus 248, 89–108.

Siebert, J., Badro, J., Antonangeli, D., and Ryerson, F. J. (2013). Terrestrial accretion under oxidizing conditions. Science, 339, 1194–1197.

Shi, C.Y., Zhang, L., Yang, W., Liu, Y., Wang, J., Meng, Y., Andrews, J.C., and Mao, W.L. (2013) Formation of an interconnected network of iron melt at Earth's lower mantle conditions. Nature Geoscience, 6, 971–975.

Takahashi, E. (1986) Melting of a dry peridotite KLB-1 up to 14 GPa: Implications on the origin of peridotitic upper mantle. Journal of Geophysical Research, 91, 9367–9382.

Trinquier, A., Birck, J.L., and Allègre, C.J., (2007) Widespread ^{54}Cr heterogeneities in the inner solar system. The Astrophysical Journal, 655, 1179–1185.

Trinquier, A., Elliott, T., Ulfbeck, D., Coath, C., Krot, A.N., and Bizzarro, M. (2009) Origin of nucleosynthetic isotope heterogeneity in the solar protoplanetary disk. Science, 324 (5925), 295–424. doi:10.1126/science.1168221.

Umemoto, K. and Hirose, K. (2020) Chemical compositions of the outer core examined by first principles calculations. Earth and Planetary Science Letters, 531, 116009, https://doi.org/10.1016/j.epsl.2019.116009.

566 Wade, J. and Wood, B.J. (2005) Core formation and the oxidation state of the Earth. Earth
567 and Planetary Science Letters, 236, 78–95.
568 Wasson, J.T. and Kallemeyn, G.W. (1988) Composition of chondrites. Philosophical
569 transactions of the Royal Society of London, A325, 535–544.
570 Wood, B.J., Wade, J., and Kilburn, M.R. (2009). Core formation and the oxidation state
571 of the Earth: Additional constraints from Nb, V and Cr partitioning. Geochimica
572 et Cosmochimica Acta, 72, 1415–1426.
573 Xie, L., Yoneda, A., Yamazaki, D., Manthilake, G., Higo, Y., Tange, Y., Guignot, N.,
574 King, A., Scheel, M., and Andrault, D. (2020) Formation of bridgmanite-
575 enriched layer at the top lower-mantle during magma ocean solidification.
576 Nature Communications, 11 (1) DOI: 10.1038/s41467-019-14071-8.
577 Zhang, J., Liebermann, R.C., Gasparik, T., and Herzberg, D. (1993) Melting and
578 subsolidus relations of SiO_2 at 9 – 14 GPa. Journal of Geophysical Research, 98,
579 19785–19793.
580 Zhang, J. Li, B., Utsumi, W., and Liebermann, R.C. (1996) In situ X-ray observations of
581 the coesite-stishovite transition: reversed phase boundary and kinetics. Physics
582 and Chemistry of Minerals, 23, 1–10.

583
584

585 **Figure captions**

586 **Figure 1.** Schematic drawing of the sample assembly. The thermocouple junction is in
587 contact with the outer surface of the Re-heater, and its terminals are taken out through the
588 edges of the MgO octahedron and the gasket.

589

590 **Figure 2.** Examples of the relations between the generated temperature up to 2500 ℃ and
591 the input power. Each colored circle denotes an individual run. The quadratic equations
592 with correlation coefficients are shown in the lower right. Each color of the equation
593 corresponds to the color of fitting curves for each experimental run.

594

595 **Figure 3.** Pressure calibration at room temperature (dashed curve) and high temperatures,
596 2500 and 2850 ℃. Orange filled circle: the datum from the calibration at 2500 ℃. The
597 result shows a generated pressure of 12.6 ± 0.9 GPa at a press load of 2.25 MN. Red filled
598 circle: the datum from the calibration at 2850 ℃. The result shows a generated pressure
599 of 13.5 ± 1.0 GPa at a press load of 2.4 MN. The calibration at room temperature was
600 undertaken by monitoring the electric resistance changes caused by the phase transitions
601 in Bi I–II (2.55 GPa), Bi III–V (7.7 GPa), GaAs (18.2 GPa), and GaP (23 GPa). At high
602 temperatures, the calibration was carried out based on the coesite–stishovite transition
603 determined by Zhang et al. (1996). Calibrated generated pressures at 2500 ℃ and 2.25
604 MN and at 2850 ℃ and 2.4 MN were 2.1 and 3.0 GPa higher than those at room
605 temperature, respectively.

606

607 **Figure 4.** Silicon image map of 1K2987 (X_{Si} = 0.61, 2500 ℃). The map area is a cross
608 section of the run product, the center (the highest *T* region) to the end (the lowest *T* region).

609 The liquid area is expanded from the center toward the right side (low-temperature side)
610 and, at the margin, contacts with Si-enriched arched zone where stishovite and liquid
611 coexisted. At a further low-temperature side, stishovite and enstatite coexisted. Liq,
612 Liquid; St, Stishovite; En, Enstatite.
613
614 **Figure 5.** Back-scattered electron image (BSEI) of 1K3138 (X_{Si} = 0.60, 2400 ℃) at the
615 low-temperature side. The molten part that shows dendritic texture contacts with the
616 enstatite-rich part formed at the lower temperature side. Liq, Liquid; En, Enstatite.
617
618 **Figure 6.** BSEI at the central high-temperature region of 1K3002 (X_{Si} = 0.70, 2500 ℃).
619 The coexistence of liquid and stishovite is displayed. Liq, Liquid; St, Stishovite.
620
621 **Figure 7.** BSEI at the central high-temperature region of 1K3157 (X_{Si} = 0.80, 2800 ℃).
622 Fine-grained crystals and the quenched liquid coexist with granular stishovite. Liq,
623 Liquid; St, Stishovite.
624
625 **Figure 8.** The melting phase relations in $MgSiO_3$–SiO_2 system at 13.5 GPa determined
626 in the present study. Open and filled circles denote liquid and solid phases, respectively.
627 Half-filled squares denote the coexistence of solid and liquid. Open and filled squares
628 denote liquid and solid compositions of the solid–liquid coexistence, respectively, which
629 are connected with tie lines. The estimated uncertainty of temperature determination is
630 shown in the lower right. Typical analytical errors in determining X_{Si} are smaller than the
631 widths of each symbol. The vertical error bars are the uncertainties in temperature

632 determinations are estimated to be ± 50 °C at ≤2500 °C and ± 120 °C at >2500 °C in the
633 case that the thermocouple was broken.
634
635 **Figure 9.** Eutectic composition (X_{Si}) vs. pressure (GPa). Eutectic compositions at 1 GPa
636 (black), 5 GPa (blue), and 13.5 GPa (red) are from Hudon et al. (2005), Dalton and
637 Presnall (1997), and this study, respectively, and others (green) are from Ozawa et al.
638 (2018). The compositional range of the enstatite chondrites from Wasson and Kallemeyn
639 (1988) is shown by the greenish-yellow band.
640
641

Table 1. Experimental conditions and results at 13.5 GPa.

Run No.	Starting composition (X_{Si})	Heating T (ºC)*	Phases present at central high T region	Composition of liquid on liquidus (Xsi)	Liquidus phase**
1K3024	0.55	2250	En+St	-----	
1K3074	0.55	2300	En+St	-----	
1K3105	0.55	2400	Liq	-----	En
1K3138	0.60	2400	Liq	-----	En
1K2987	0.61	2500	Liq	-----	St
1K3002	0.70	2500	Liq+St	0.60†	
1K3129	0.70	2700	Liq+St	0.69†	
1K3157	0.80	2800	Liq+St	0.72†	
1K3178	0.90	3180<	Liq+(La+Cr+Re)‡	n.d.	
1K3204	1.00	2800	St	-----	
1K3207	1.00	2900	Coe	-----	

*Uncertainties: ±50 ºC at ≤2500 ºC and ±120 ºC at >2500 ºC.

**Liquidus phase was determined from microscopic observation and X-ray deffractometry.

†Totals of chemical analysis of the liquids in 1K3002, 1K3129 and 1K3157 are 99.93, 99.93 and 98.28 wt.%, respectively. En: Enstatite, St: Stishovite, Liq: Liquid. (La+Cr+Re)‡ means contaminants of those elements. n.d.: not determined

This is the peer-reviewed, final accepted version for American Mineralogist, published by the Mineralogical Society of America.
The published version is subject to change. Cite as Authors (Year) Title. American Mineralogist, in press.
DOI: https://doi.org/10.2138/am-2022-8004. http://www.minsocam.org/

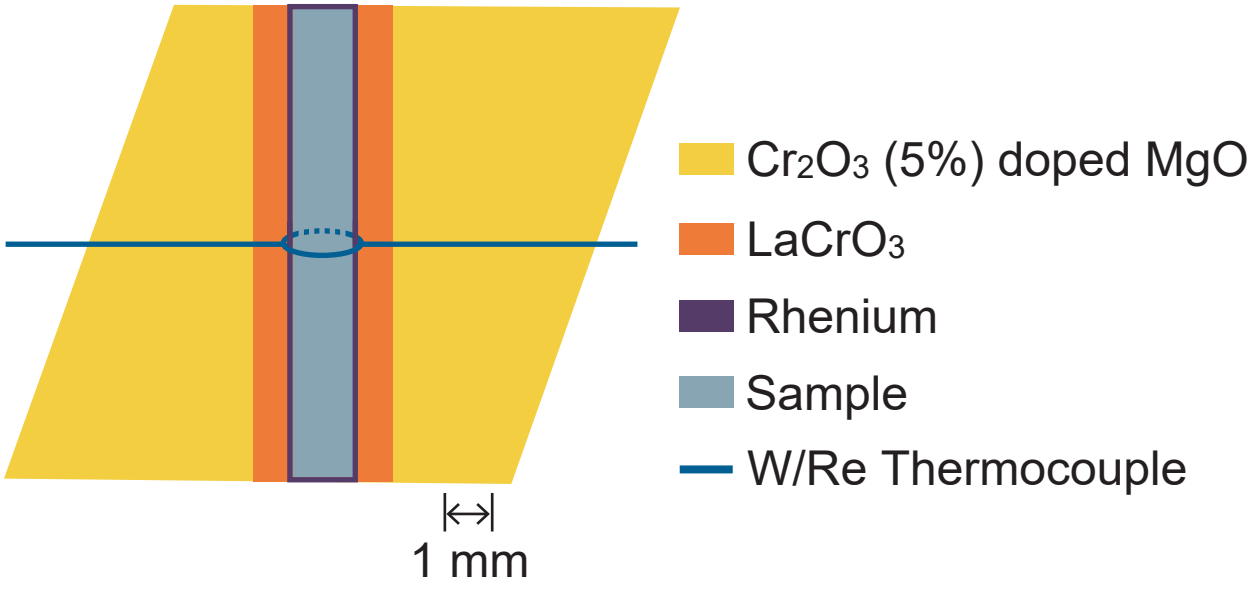

Fig. 1

Moriguti et al. (2021)

This is the peer-reviewed, final accepted version for American Mineralogist, published by the Mineralogical Society of America.
The published version is subject to change. Cite as Authors (Year) Title. American Mineralogist, in press.
DOI: https://doi.org/10.2138/am-2022-8004. http://www.minsocam.org/

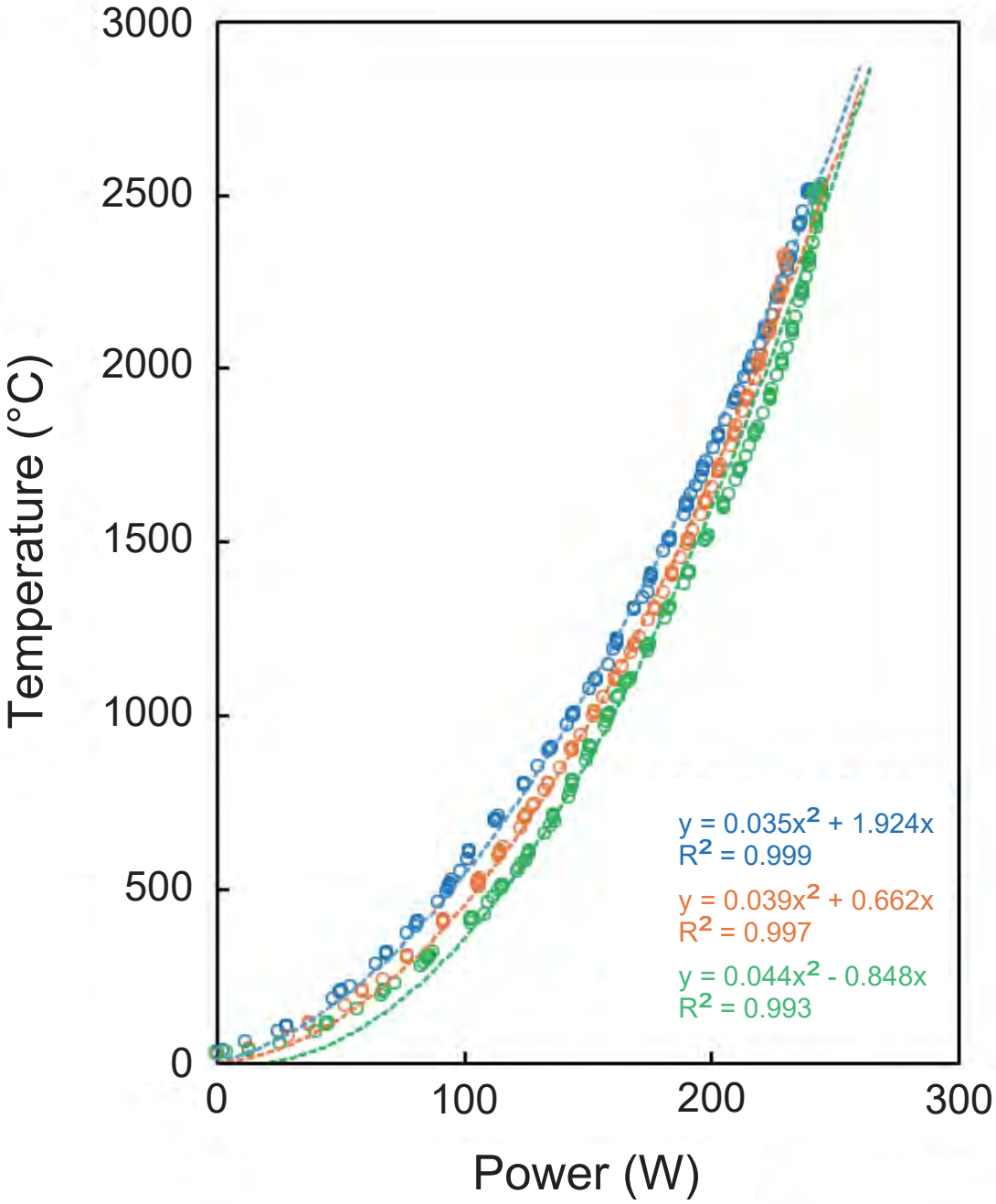

Fig. 2

Moriguti et al. (2021)

This is the peer-reviewed, final accepted version for American Mineralogist, published by the Mineralogical Society of America.
The published version is subject to change. Cite as Authors (Year) Title. American Mineralogist, in press.
DOI: https://doi.org/10.2138/am-2022-8004. http://www.minsocam.org/

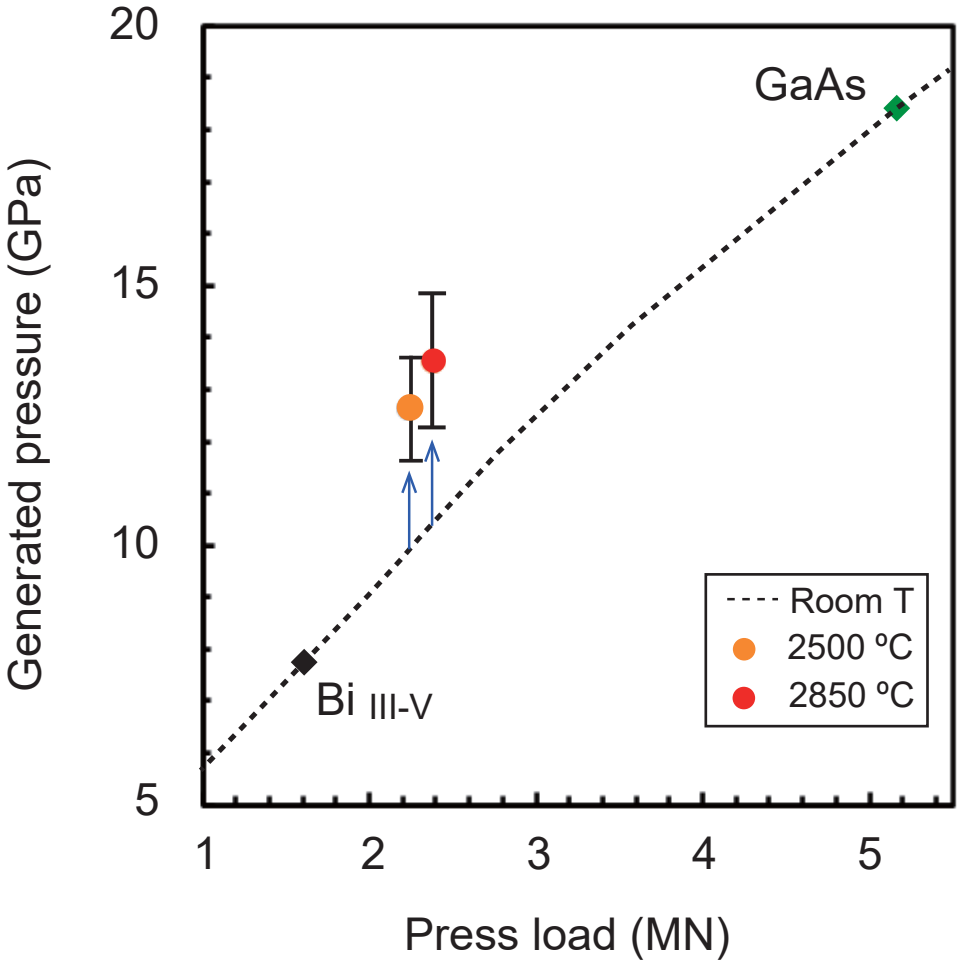

Fig. 3

Moriguti et al. (2021)

This is the peer-reviewed, final accepted version for American Mineralogist, published by the Mineralogical Society of America.
The published version is subject to change. Cite as Authors (Year) Title. American Mineralogist, in press.
DOI: https://doi.org/10.2138/am-2022-8004. http://www.minsocam.org/

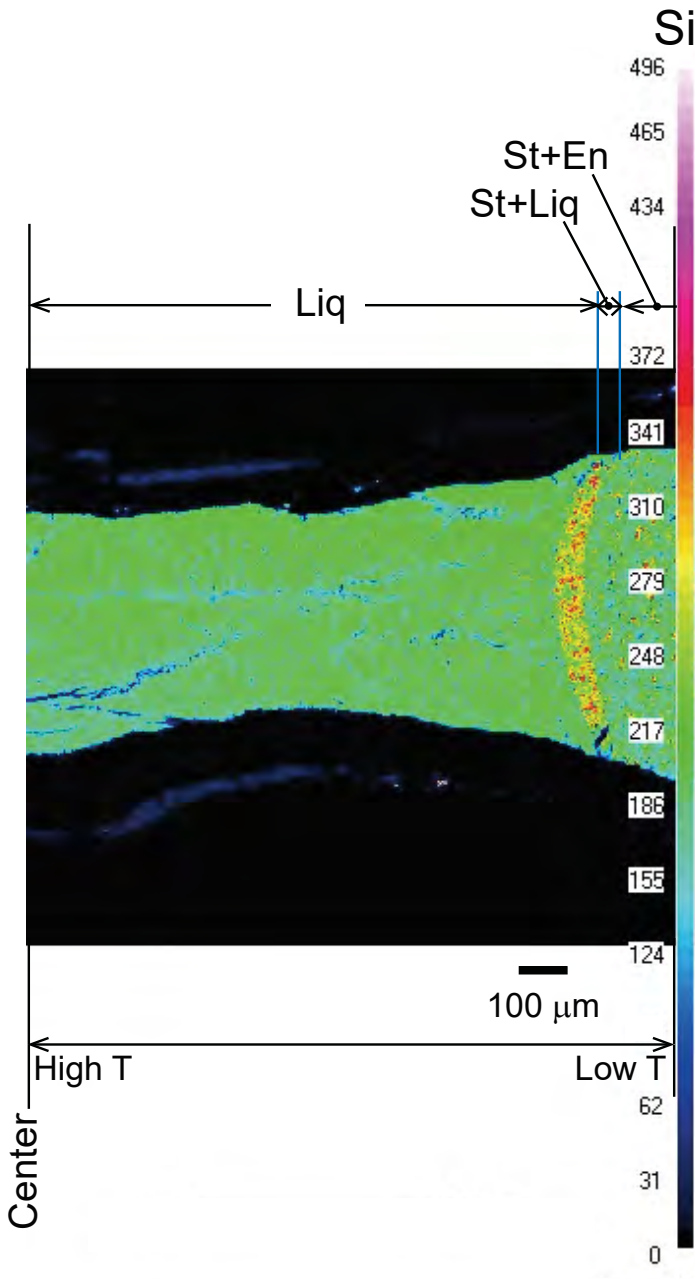

Fig. 4

Moriguti et al. (2021)

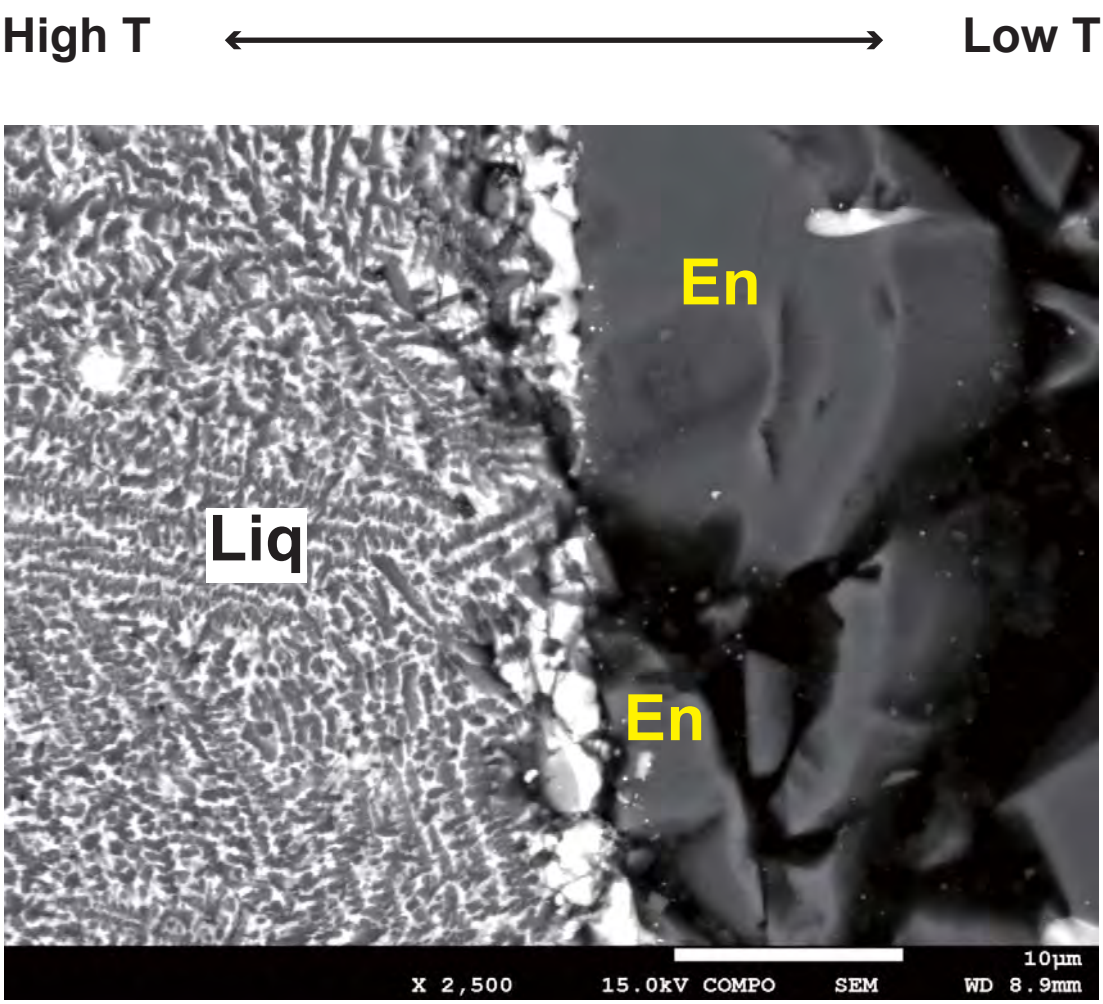

Fig. 5

Moriguti et al. (2021)

Center of the run product

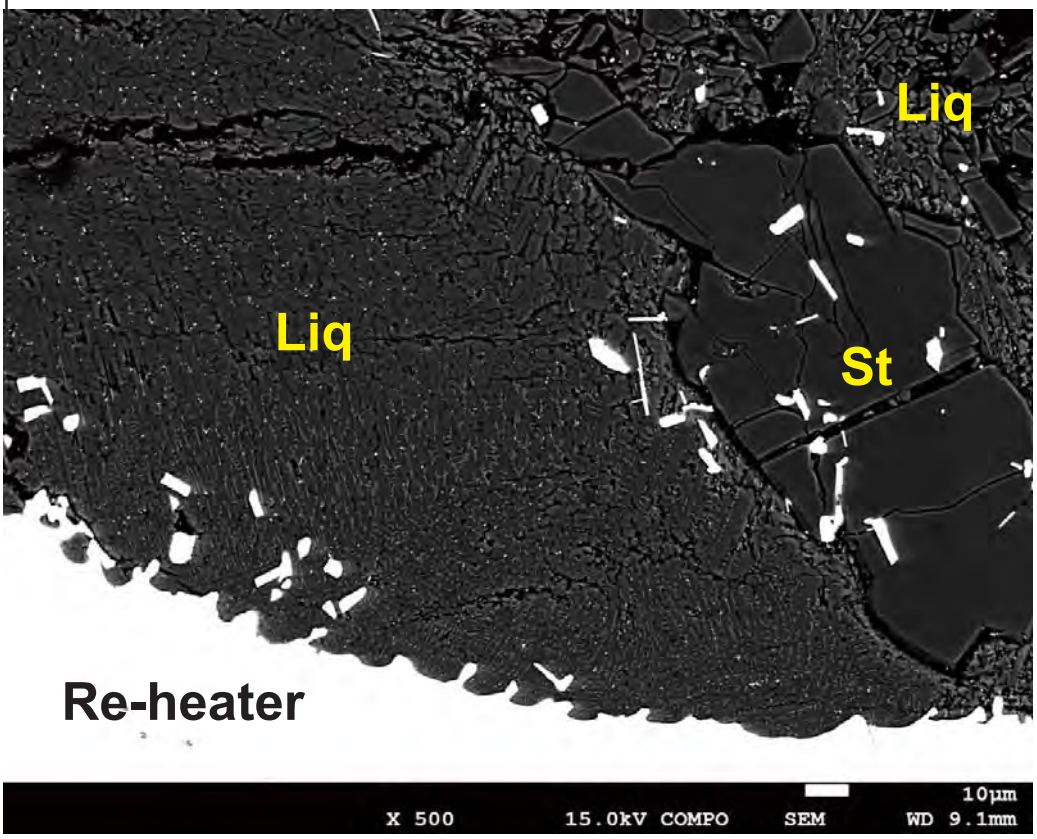

Fig. 6

Moriguti et al. (2021)

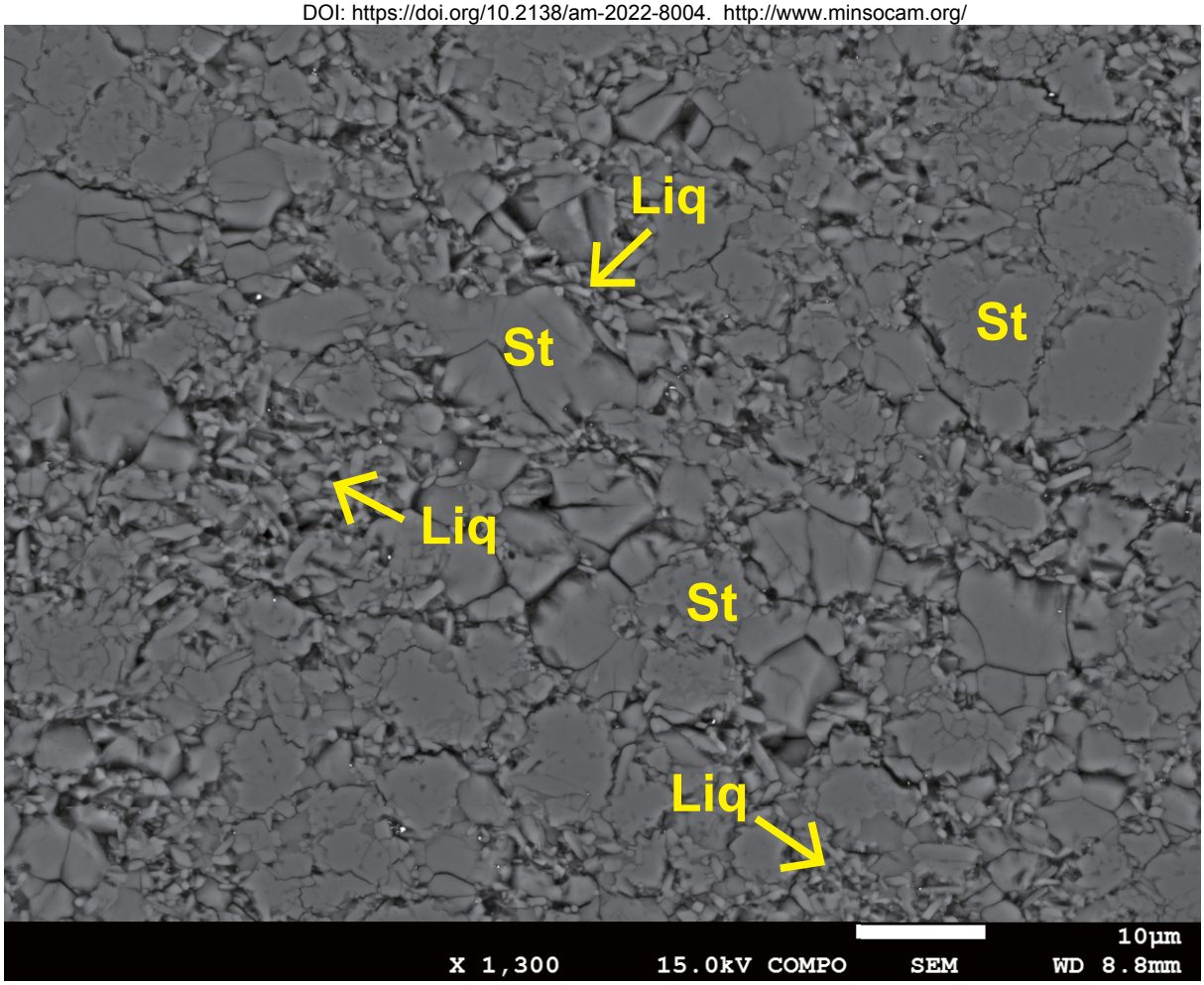

Fig. 7

Moriguti et al. (2021)

This is the peer-reviewed, final accepted version for American Mineralogist, published by the Mineralogical Society of America.
The published version is subject to change. Cite as Authors (Year) Title. American Mineralogist, in press.
DOI: https://doi.org/10.2138/am-2022-8004. http://www.minsocam.org/

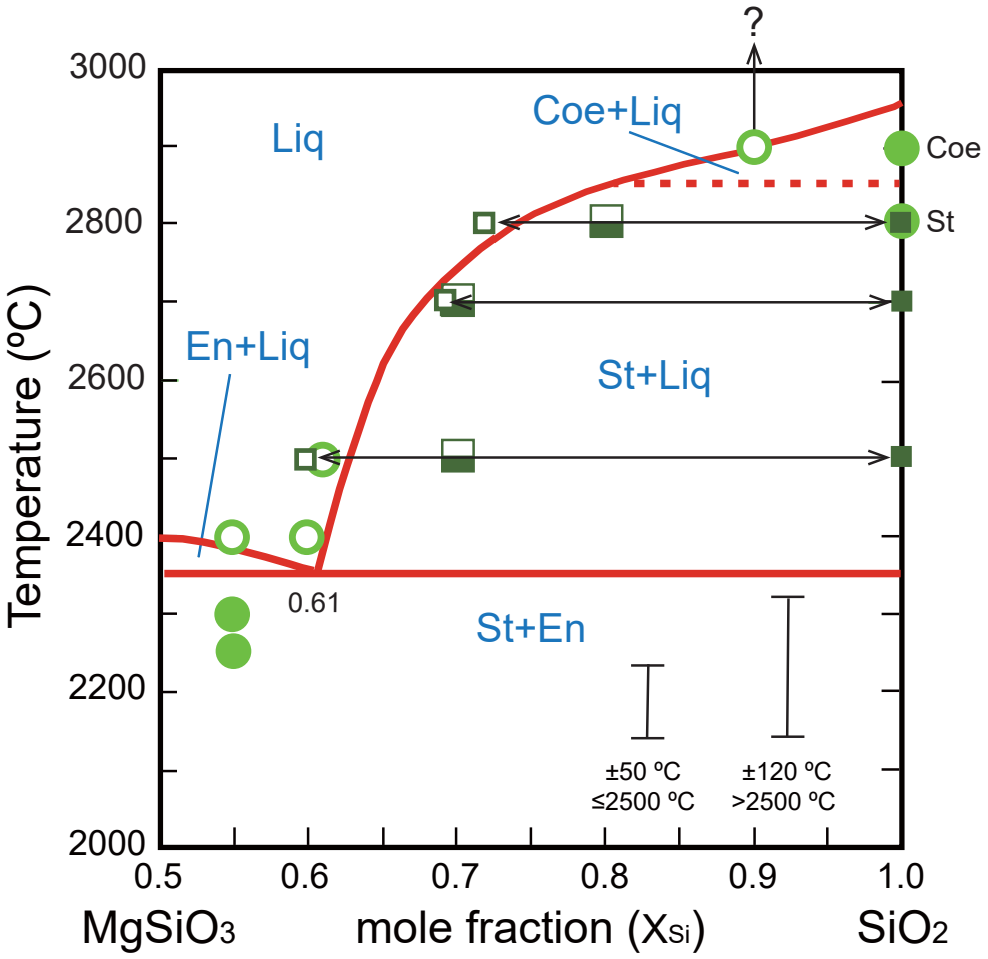

Fig. 8

Moriguti et al. (2021)

This is the peer-reviewed, final accepted version for American Mineralogist, published by the Mineralogical Society of America.
The published version is subject to change. Cite as Authors (Year) Title. American Mineralogist, in press.
DOI: https://doi.org/10.2138/am-2022-8004. http://www.minsocam.org/

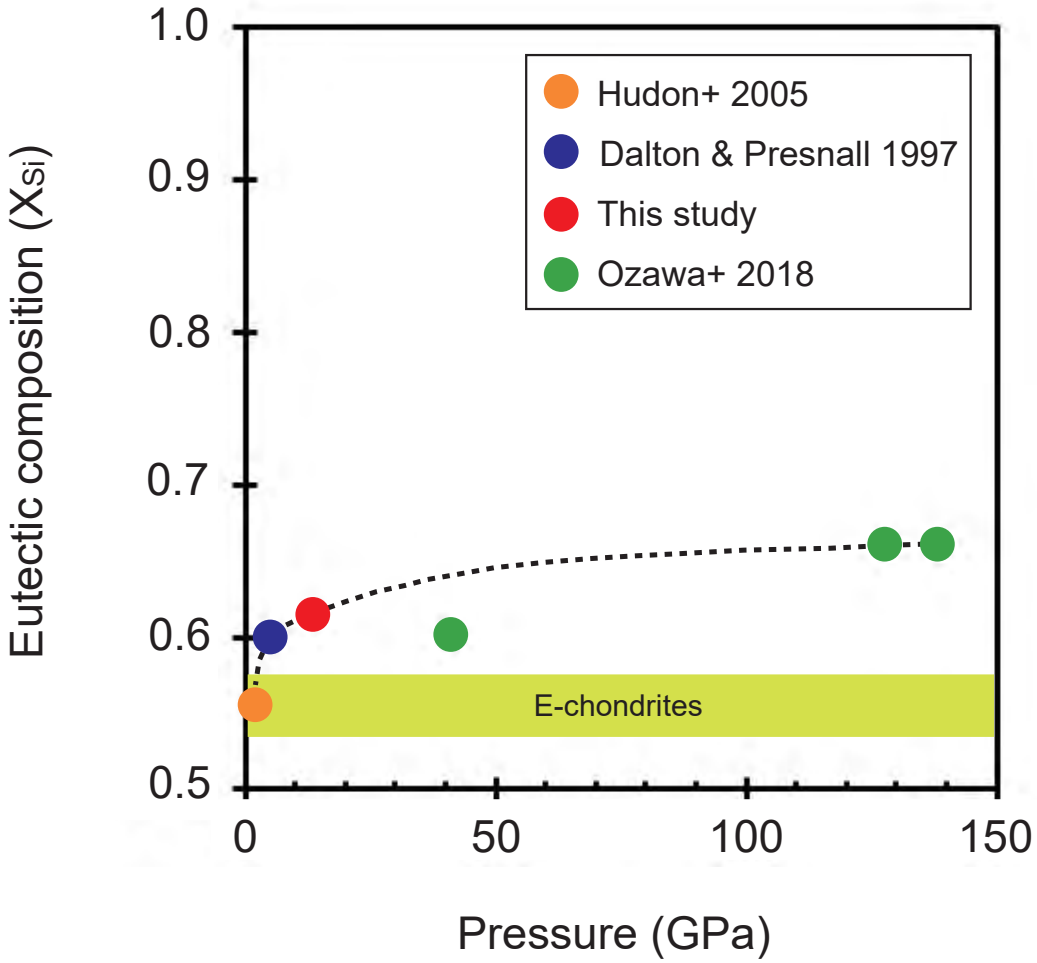

Fig. 9

Moriguti et al. (2010)